ARTICLES
https://doi.org/10.1038/s41560-018-0200-6
nature energy

A fluorene-terminated hole-transporting material for highly efficient and stable perovskite solar cells

Nam Joong Jeon[1,4], Hyejin Na[1,4], Eui Hyuk Jung[1,4], Tae-Youl Yang[1], Yong Guk Lee[1], Geunjin Kim[1], Hee-Won Shin[2], Sang Il Seok[1,3], Jaemin Lee[1*] and Jangwon Seo[1*]

Perovskite solar cells (PSCs) require both high efficiency and good long-term stability if they are to be commercialized. It is crucial to finely optimize the energy level matching between the perovskites and hole-transporting materials to achieve better performance. Here, we synthesize a fluorene-terminated hole-transporting material with a fine-tuned energy level and a high glass transition temperature to ensure highly efficient and thermally stable PSCs. We use this material to fabricate photovoltaic devices with 23.2% efficiency (under reverse scanning) with a steady-state efficiency of 22.85% for small-area (~0.094 cm^2) cells and 21.7% efficiency (under reverse scanning) for large-area (~1 cm^2) cells. We also achieve certified efficiencies of 22.6% (small-area cells, ~0.094 cm^2) and 20.9% (large-area, ~1 cm^2). The resultant device shows better thermal stability than the device with spiro-OMeTAD, maintaining almost 95% of its initial performance for more than 500 h after thermal annealing at 60 °C.

Over the past few years, hybrid inorganic–organic perovskite solar cells (PSCs) have attracted significant amounts of attention due to their photo-physical properties, the potential for low-cost solution fabrication processing, and their high power conversion efficiency (PCE), which presently exceed 22%[1–11]. Most highly efficient PSCs utilize an n-type layer of mesoporous TiO_2 and a p-type layer of spiro-OMeTAD (or PTAA) in the n-i-p device configuration, where formamidinium (FA)-cation-based perovskite materials are widely used as light absorbers. We previously reported a mixed perovskite of $(FAPbI_3)_{0.85}(MAPbBr_3)_{0.15}$ via composition engineering to stabilize the 'black' phase of the $FAPbI_3$-based perovskite with a bandgap of ~1.54 eV from the 'yellow' phase of a non-photoactive isomer[7]. Recently, Cs or Rb was incorporated into FA/methylammonium (MA) mixtures to improve the photovoltaic performance and stability of PSCs[12–15]. For the Rb/Cs/FA/MA-containing perovskite, a high open-circuit voltage (V_{OC}) of 1.24 V at a bandgap (E_g) of 1.63 eV was obtained to yield a PCE of 21.6%, leading to a loss-in-potential (difference between V_{OC} and E_g) of 0.39 V, comparable to that (~0.4 V) of silicon solar cells[15]. Nevertheless, better performance in PSCs requires greater light harvesting to enhance the photocurrent.

Very recently, we prepared a mixed perovskite of $(FAPbI_3)_{0.95}(MAPbBr_3)_{0.05}$ with a bandgap of 1.51 eV and successfully reduced the trap concentration of bulk perovskite film by the addition of triiodide ions (I_3^-)[9]. This approach to eliminate the deep-level traps responsible for non-radiative recombinations within the bulk perovskite film is crucial for reducing the open-circuit voltage loss. The resultant device exhibited a PCE of 22.1% with a high V_{OC} of 1.11 V and a high current density (J_{SC}) of 25 mA cm^{-2}. This current can be nearly identical to the maximum value converted from a light absorber with a bandgap of 1.51 eV into current. In addition, a wide range of attempts to achieve a defect-free perovskite film have been made to date. These include passivating the surface, increasing the grain size, reducing the grain boundaries and adjusting the crystal dimensions of the perovskite film[16–19].

In addition to perovskite layers, interface-material-dependent losses can also be a determining factor that limits the V_{OC} of devices rather than nonradiative bulk recombination losses, even if a defectless perovskite film is suitably prepared to reach the maximal values of J_{SC} and fill factor (FF) beyond the theoretical limits. Thus, for further improvements of device performance capabilities, more efforts to maximize the built-in-potential and enhance V_{OC} in PSCs are necessary by utilizing selective charge-transporting materials with a suitable energy level and balanced charge transport efficacy.

Recent research systematically studied the relationship between the highest occupied molecular orbital (HOMO) energy levels of hole-transporting materials (HTMs) and the photovoltaic parameters, especially V_{OC}, for spirobifluorene-based derivatives, fluorene–dithiophene derivatives and tetraphenyl–arylamine derivatives, respectively[20–22]. A higher V_{OC} is observed with a higher oxidation potential for HTMs when the driving force for hole injection is satisfactory. However, multiple aspects of HTMs, such as the intrinsic charge mobility, dopant-additive optimization for high conductivity, and specific interaction with the surface of the perovskite can cause complicated effects with regard to the ionization potentials (IPs) of HTMs on the V_{OC} values of PSCs. For this reason, the top level of performance from a device utilizing a new HTM has rarely been reported, despite the fact that a tremendous number of HTMs have been developed and applied to PSCs in recent years[23–30]. Thus, only a few new HTMs can be found to exhibit higher V_{OC} and higher PCE values than the best device using spiro-OMeTAD. More importantly, enhanced thermal stability of solar cells is also necessary for the commercialization of PSCs. As reported in the literature, most devices employing spiro-OMeTAD as a HTM are associated with severe degradation against thermal stress because the additives resulted in a significant drop in T_g of the HTM[31,32]. This highlights

---

[1] Division of Advanced Materials, Korea Research Institute of Chemical Technology (KRICT), Daejeon, South Korea. [2] Department of Energy Science, Sungkyunkwan University, Suwon, South Korea. [3] School of Energy and Chemical Engineering, Ulsan National Institute of Science and Technology (UNIST), Ulsan, South Korea. [4] These authors contributed equally: Nam Joong Jeon, Hyejin Na, Eui Hyuk Jung. *e-mail: jminlee@krict.re.kr; jwseo@krict.re.kr

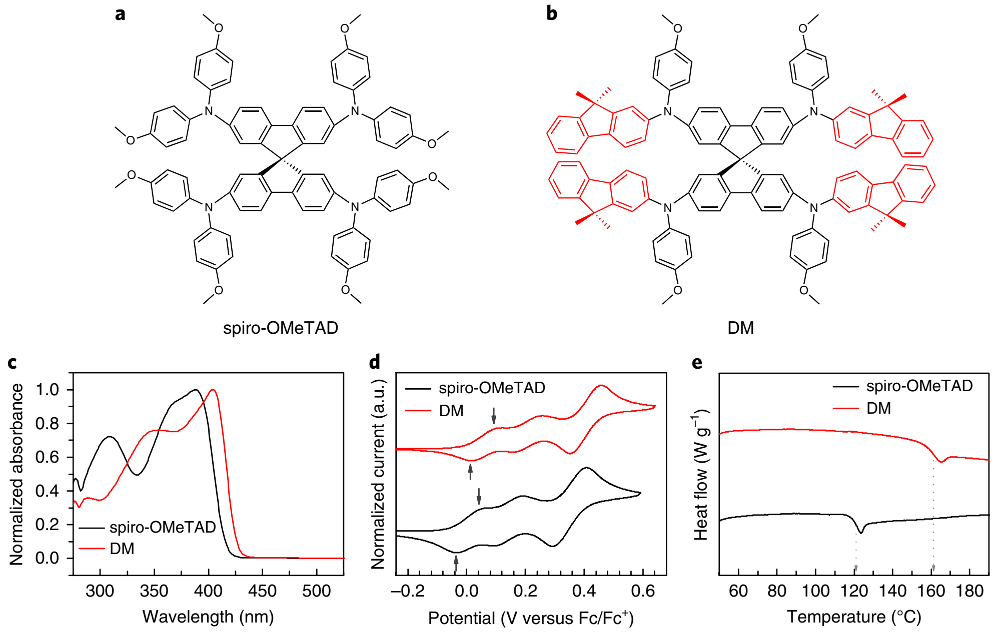

Fig. 1 | Optical, electrochemical and thermal characteristic of HTMs. a,**b**, Chemical structures of spiro-OMeTAD (**a**) and DM (**b**). **c**, Ultraviolet–visible absorption spectra of spiro-OMeTAD and DM in the solid state. **d**, Cyclic voltammograms of spiro-OMeTAD and DM. The downward arrows indicate the first peak anodic potentials, and the upward arrows indicate the first peak cathodic potentials. **e**, DSC curves of spiro-OMeTAD and DM. The vertical dashed lines indicate the glass transition temperature.

the need for the development of thermally stable alternative HTMs capable of high-performance outcomes in the presence of additives.

In this work, we synthesize a fluorene-terminated HTM (N^2,$N^{2'}$,N^7,$N^{7'}$-tetrakis(9,9-dimethyl-9H-fluoren-2-yl)-N^2,$N^{2'}$,N^7,$N^{7'}$-tetrakis(4-methoxyphenyl)-9,9′-spirobi[fluorene]-2,2′,7,7′-tetraamine) (which we abbreviate to DM) as a model system with a fine-tuned HOMO level in an effort to enhance the V_{OC} value and realize a high glass transition temperature T_g (~160 °C) for thermally stable PCSs. We also prepare a high-quality film sample consisting of a mixed perovskite based on $(FAPbI_3)_{0.95}(MAPbBr_3)_{0.05}$ which has a grain size of 300~1,000 nm. The DM-based device exhibits a large degree of variation in the PCE according to the amount of additive used. The optimized condition led to a higher PCE owing to the higher V_{OC} relative to that of a device made with spiro-OMeTAD. The champion device with DM as a HTM shows a PCE of 23.2% with a J_{SC} of 24.9 mA cm^{-2}, FF equal to 81% and a V_{OC} of 1.14 V (under reverse scanning). We achieve a certified PCE of 22.6% from the resultant device. We also show a large device with an aperture area of ~1 cm^2 which reached a PCE of 21.7% (under reverse scanning) and a certified PCE of 20.9%. Furthermore, the device with DM shows good long-term stability for 500 h after annealing at 60 °C, whereas the device with spiro-OMeTAD degraded rapidly after only 50 h.

Material characteristics

Figure 1a,b depicts the chemical structures of spiro-OMeTAD and DM. The synthetic details are given in Supplementary Figs. 1–5. Though most of the recent development of high-performance HTMs has been mainly focused on the development of new central core structures[23–26], what determines the physical and opto-electronic properties of the HTMs is the conjugated structure of such core and peripheral units[33,34]. The peripheral structure is therefore of equal importance to finely tune the properties of the HTMs. With respect to the molecular design of the HTM, we maintained the well-established spirobifluorene core and introduced a fluorene unit as a new peripheral group instead of *p*-anisole for spiro-OMeTAD. DM was simply synthesized via two consecutive Buchwald–Hartwig amination reactions using commercially available 2,2′,7,7′-tetrabromo-9,9′-spirobifluorene, *p*-anisidine and 2-bromo-9,9-dimethylfluorene.

Figure 1c shows the absorption spectra of the HTMs; a slight shift to a longer wavelength with regard to the absorption onset for the DM sample probably stemmed from an extended π-conjugation through the fluorene unit compared to the simple *p*-anisole of spiro-OMeTAD. This is supported by the molecular simulation results (see Supplementary Fig. 6), which show that the electron density of the lowest unoccupied molecular orbital (LUMO) of DM is more widely distributed in the fluorene part. An additional electrochemical analysis by cyclic voltammetry (CV) was also conducted, as shown in Fig. 1d. Interestingly, the change of the peripheral unit of the HTM from *p*-anisole to dimethylfluorene resulted in a slightly increased oxidation potential. Regarding the HOMO level of spiro-OMeTAD as −5.22 eV, the HOMO level of DM was calculated to be −5.27 eV (ref. [33]). The LUMO levels of the HTMs were also estimated by combining the HOMO level and the optical bandgap values. Thus, the LUMO levels for DM and spiro-OMeTAD corresponded to −2.36 and −2.24 eV, respectively. Next, Fig. 1e shows the differential scanning calorimetry (DSC) thermograms of the DM and spiro-OMeTAD; the T_g clearly increases for DM, reaching 161 °C, which is nearly 40 °C higher than that of spiro-OMeTAD. The increased T_g of the HTM is beneficial with regard to the stability of the resultant devices. In addition to the DSC results, the thermogravimetric analysis (TGA) results also clearly show that the introduction of the fluorene unit into DM improved the thermal stability of the HTM itself (see Supplementary Fig. 7). The physical characteristics of DM and spiro-OMeTAD are summarized in Table 1.

Photovoltaic performance

To evaluate DM as a HTM for PSCs, we fabricated a $FAPbI_3$-based PSC based on the typical bilayered device configuration consisting of a fluorine-doped tin-oxide (FTO) substrate/blocking layer bl-TiO_2/mp-TiO_2/$(FAPbI_3)_{0.95}(MAPbBr_3)_{0.05}$/HTM/Au. Following our solvent-engineering process, we prepared a dense

Table 1 | Optical, electrochemical and thermal properties of spiro-OMeTAD and DM

	λ_{max} (nm)	E_g (eV)	HOMO (eV)	LUMO (eV)	T_g (°C)	T_{d95} (°C)[a]
spiro-OMeTAD	388	2.98	−5.22	−2.24	121	437
DM	404	2.91	−5.27	−2.36	161	460

[a] T_{d95} denotes the degradation temperature with 5% weight loss.

and flat perovskite-absorbing layer on the mp-TiO_2 scaffold and subsequently deposited DM on top of the perovskite film via spin-coating. Figure 2a shows a cross-sectional SEM image of the perovskite film. Grain sizes ranging from 300 to 1,000 nm were observed, together with a dense film morphology and full surface coverage in the absence of voids (see Supplementary Fig. 8). The film thickness of the perovskite is in the range 500–600 nm. Thus, the average grain sizes are comparable to the film thickness, which is favourable for charge extraction. That is, the photoinduced charges can move in the out-of-plane direction across the HTM towards the electrode without crossing the grain boundaries. The fabricated film using MACl exhibited two typical perovskite XRD peaks at 14° and 28°, indicating the successful formation of the perovskite based on the composition of $(FAPbI_3)_{0.95}(MAPbBr_3)_{0.05}$ (see Supplementary Fig. 8). In contrast, no use of MACl resulted in a poor performance of the device, as reported in our previous literature[7].

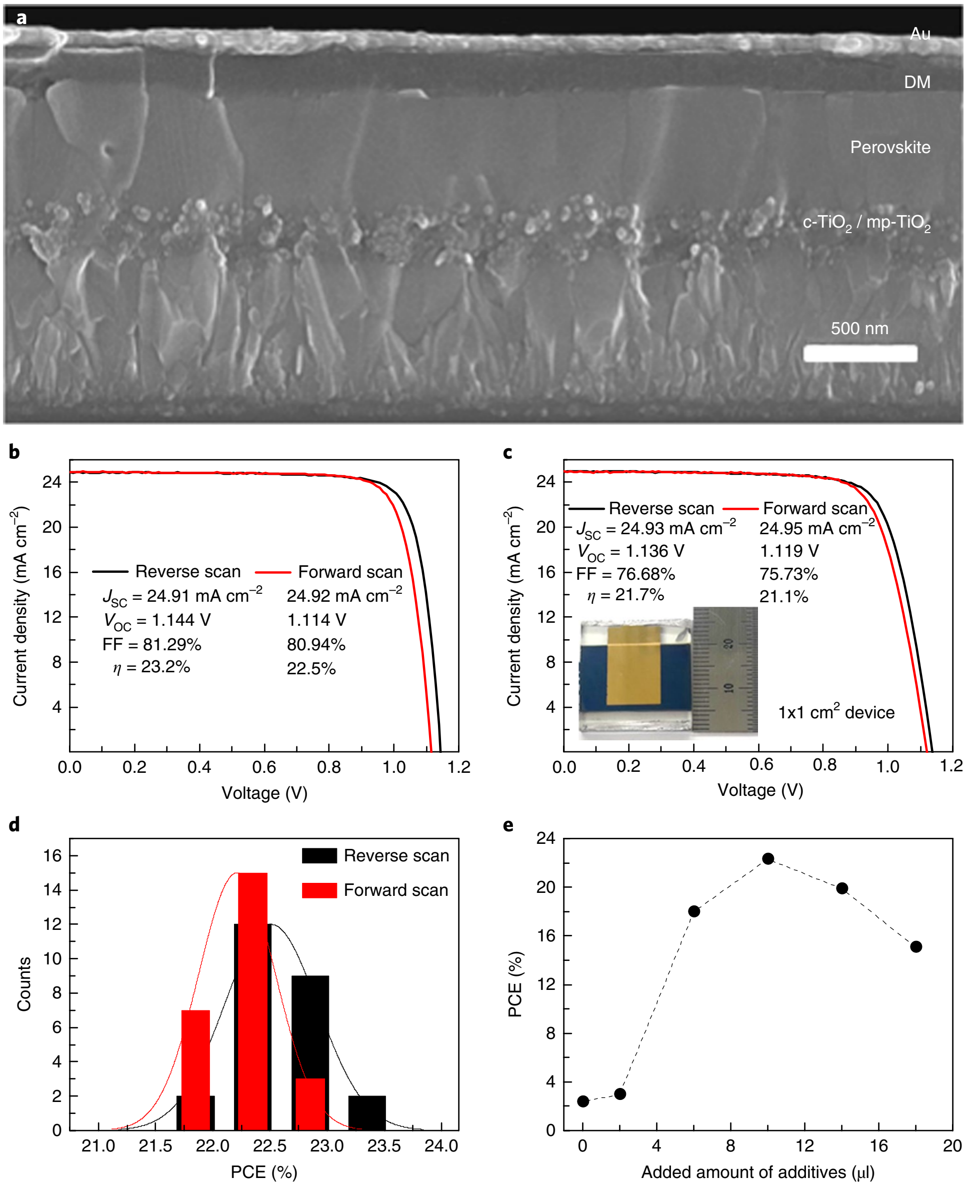

Fig. 2 | Performance and device structure of perovskite solar cells using spiro-OMeTAD and DM. a, Cross-sectional scanning electron microscopy (SEM) image of perovskite solar cells. **b**, *J*–*V* curves measured by reverse and forward scans of the best cell using DM with active area of 0.0939 cm^2. **c**, *J*–*V* curves of DM-based device with active area of 0.991 cm^2. The inset shows the upper side of 1 × 1 cm^2 DM-based device. **d**, PCE histograms of 25 devices using DM with active area of 0.0939 cm^2 measured along reverse and forward scan directions. The average PCEs are 22.4% (reverse scan) with a standard deviation (σ) of 0.41 and 22.2% (forward scan) with σ of 0.34. **e**, Relationship between the power conversion efficiency and the amount of additive added to the DM. The added amount of additives indicates the sum amount of Li-TFSI solution in acetonitrile (340 mg ml^{-1}) and pure *t*BP with 1:1 volume ratio.

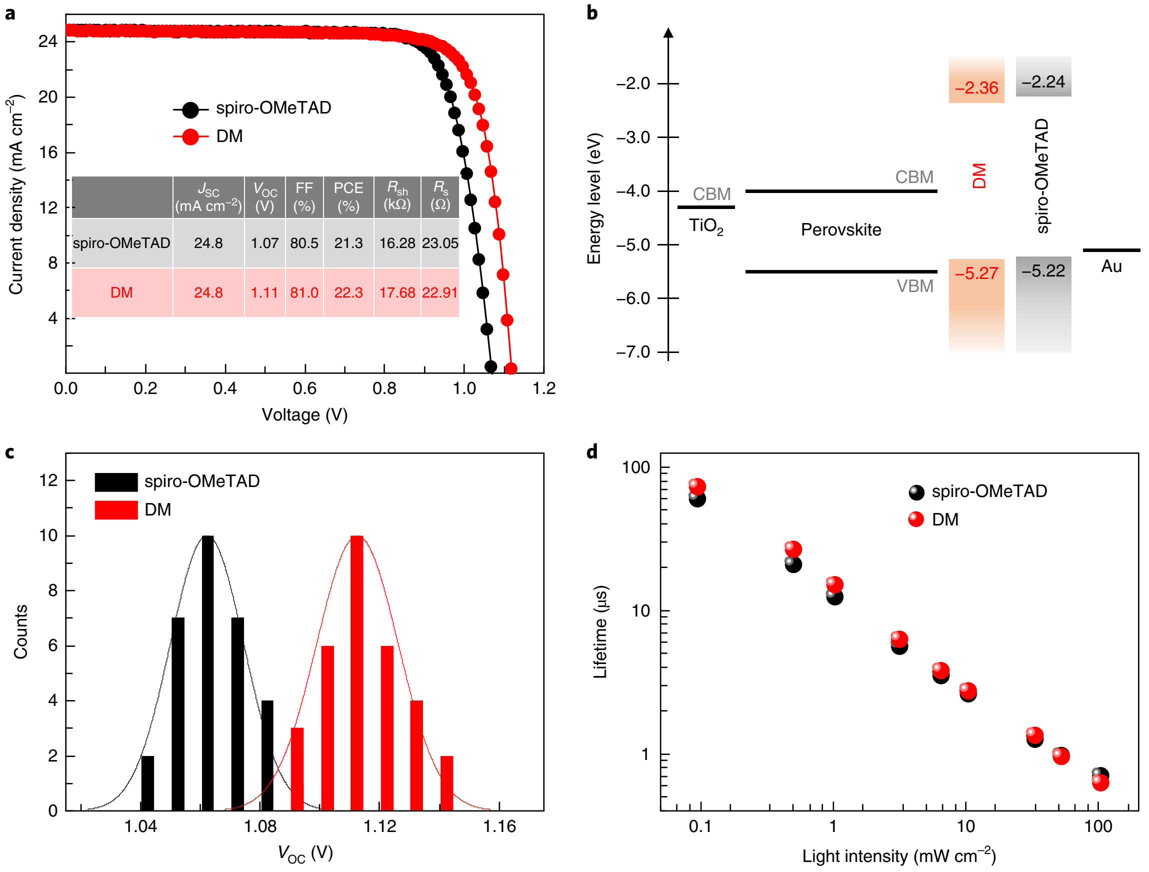

Fig. 3 | Photovoltaic performance outcomes of perovskite cells using DM. **a**, *J–V* curves of the average measured efficiency for the spiro-OMeTAD and DM perovskite devices. **b**, Energy level diagram of DM and spiro-OMeTAD. CBM and VBM denote conduction band minimum and valence band maximum, respectively. **c**, Histogram of the solar cell average V_{oc} value of 31 devices. The average V_{OC} values are 1.06 V (spiro-OMeTAD) with a standard deviation (σ) of 0.0137 and 1.11 V (DM) with a σ of 0.0123. **d**, Charge recombination lifetimes of devices with spiro-OMeTAD and DM as measured by the transient photovoltaic method as a function of the bias light intensity.

The best-performing cell with a small area of 0.0939 cm^2 exhibited a high PCE of 23.2% (J_{SC} = 24.91 mA cm^{-2}, V_{OC} = 1.144 V, FF = 81.29%) with slight hysteresis behaviour, as displayed in Fig. 2b. The steady-state PCE corresponded to 22.85% (see Supplementary Fig. 9). This device produced a certified PCE of 22.6% owing to the enhanced V_{OC} (see Supplementary Fig. 10). We also prepared a large-area cell (0.991 cm^2), demonstrating a PCE of 21.7% (J_{SC} = 24.93 mA cm^{-2}, V_{OC} = 1.136 V, FF = 76.68%) and a certified PCE of 20.9 %, as shown in Fig. 2c and Supplementary Fig. 11. The statistical distribution of the PCE for small-area devices is shown in Fig. 2d. To the best of our knowledge, the certified PCEs of 20.9% for large cells (1 × 1 cm^2) represent the highest efficiency among PSCs reported thus far.

Table 2 | Photovoltaic performance outcomes of cells fabricated using DM with various amounts of the additive

Li-TFSI + *t*BP (μl)	J_{SC} (mA cm^{-2})	V_{OC} (V)	FF (%)	*η* (%)
0	14.3	0.92	18.2	2.4
2	16.1	1.02	18.6	3.1
6	24.5	1.05	70.1	18.0
10	24.7	1.11	81.0	22.2
14	24.7	1.05	76.9	19.9
18	23.6	0.95	67.3	15.1

Li-TFSI + *t*BP means the sum amount of Li-TFSI solution (340 mg ml^{-1}) and pure *t*BP with a 1:1 volume ratio.

Such high efficiencies of PCE are achieved by the careful optimization of the HTL composition. We investigated the effect of different amounts of additives (Li-TFSI and *t*BP) on the device performance outcomes with the DM-containing HTL and summarized the corresponding photovoltaic results, as shown in Fig. 2e and Table 2. Without additives, or with only small amounts of additives, the PCE of the device is very low because the conductivity of DM is not high enough to transport the injected holes through ~150-nm-thick HTL to the Au electrode, causing severe charge recombination and a very low FF, together with reductions in J_{SC} and V_{OC}. By increasing the amount of the additive to 10 μl, the PCE increases as the FF increases, but past an addition of additives of 14 μl, the efficiency drops abruptly due to the large decreases in FF and V_{OC}. Such a decrease in the PCE is associated with the morphology of the HTM; with a high amount of additives, many more voids in the film are clearly observed (see Supplementary Fig. 12). This is probably the main cause of the migration of the metal into the HTM or the diffusion of the additives into the perovskite layer. By carefully adjusting the amount of additives inside the HTL, we could find the optimization condition that maximized hole extraction in the device. The optimized device exhibited a PCE of 22.3% with a J_{SC} value of 24.8 mA cm^{-2}, a V_{OC} value of 1.11 V and a FF equal to 81%, as shown in Fig. 3a. The statistical distribution of the PCE as displayed in Fig. 2d revealed high repeatability of the device performance.

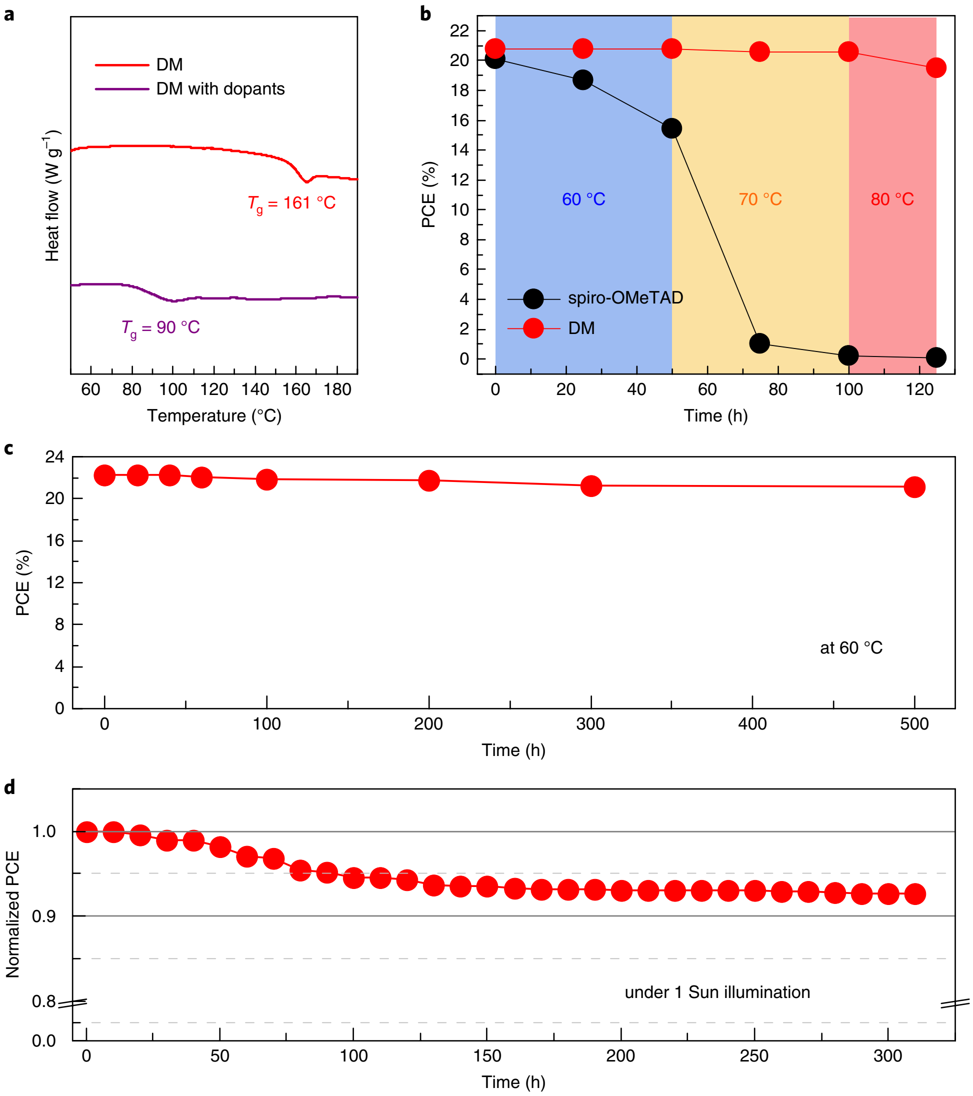

Fig. 4 | Thermal and photostability of perovskite cells using DM. a, DSC curves of the DM powder with and without dopants. **b**, Stability of the devices stressed at different temperatures of 60, 70 and 80 °C in air (~25% RH) with DM and spiro-OMeTAD. **c**, Long-term thermal stability of the device stressed at 60 °C hot plate in air (~25% RH) and dark condition employing DM. Initial device: J_{SC} = 24.8 mA cm^{-2}, V_{OC} = 1.12 V, FF = 80.3% and PCE = 22.3%; device after 500 h: J_{SC} = 24.5 mA cm^{-2}, V_{OC} = 1.11 V, FF = 78.0%, and PCE = 21.2%. **d**, Evolution of normalized power conversion efficiency obtained from DM-based device with encapsulation under maximum power point tracking and continuous light irradiation (AM 1.5 G, 100 mW cm^{-2}, white LED) at 25 °C. Initial efficiency is 20.8% with a J_{SC} of 24.3 mA cm^{-2}, a V_{OC} of 1.11 V and a FF of 76.8%, which were measured from J–V curves.

It also showed that the PCE of the best cell exceeded 23%, as mentioned above.

The device using DM as a HTM showed better performance due to a higher V_{OC} as compared to the device using spiro-OMeTAD, as shown in Fig. 3a. With respect to J_{SC} and FF, the two devices showed nearly identical values. This outcome is related to the similar order of the mobility for DM and spiro-OMeTAD according to space-charge-limited current (SCLC) measurements (see Supplementary Fig. 13). Time-resolved photoluminescence measurement was carried out to elucidate the dynamics of charge transfer occurring at the perovskite/HTM interfaces. As shown in Supplementary Fig. 14 and Supplementary Table 1, the pristine perovskite film showed a relatively long PL lifetime of 407.5 ns. In case of HTM-coated perovskite films, PL lifetimes decreased greatly, with values of 31.2 and 16.7 ns for the spiro-OMeTAD and DM-coated film, respectively. In general, a shorter lifetime is attributed to a better charge extraction by a hole-accepting layer contacting the perovskite film. Thus, we consider that DM has a comparable charge-extracting ability to spiro-OMeTAD. In addition, we found that the shunt and the series resistance values are similar in the two devices. It is important to note that we used perovskite films fabricated via an identical process and that both HTMs had comparable charge transport properties with respect to the mobility. The condition under which the additives were added was optimized for each HTM in the PSCs. With respect to the band alignment, the HOMO energy levels of each HTM are given in Fig. 3b, implying that DM has a slightly lower HOMO energy level by 0.05 eV than that of spiro-OMeTAD. From photoelectron spectroscopy measurements, a similar trend was also found in Supplementary Fig. 15. This may be related to the histogram of the V_{OC} distribution shown in Fig. 3c, which clearly indicated that a higher built-in voltage was established when spiro-OMeTAD was replaced with DM.

To gain more insight into the recombination behaviour of a full device, we carried out transient photovoltage decay measurements under the open-circuit voltage, as shown in Fig. 3d. As a function of the light intensity, the recombination lifetimes (τ) for each device with spiro-OMeTAD and DM are nearly identical. No evidence of any change in the defect states related to the bulk or the interfacial recombinations is likely to be found when the light-absorbing perovskite film comes into contact with the HTM in each case. That is, photogenerated holes can be injected into the HTM without significant interfacial recombinations and travel towards Au with no considerable trapping across the HTM layer that would cause reductions in the J_{SC} and FF values. For this reason, both devices exhibited excellent behaviour with regard to J_{SC} and FF, as high as ~24.8 mA cm^{-2} and ~0.80, respectively. In contrast, the distinguished difference among the photovoltaic parameters was only V_{OC}, which is the main factor determining the PCE of the device, as shown in Fig. 3c and Supplementary Fig. 16. As noted above, this is associated with the replacement of the methoxyphenyl moiety by its dimethylfluorene counterpart, which would weaken the electron-donating power considering the molecular design. Compared to spiro-OMeTAD, the HOMO energy level of DM is closer to the valence band of the perovskite, which can favourably increase the built-in voltage at the junction of the device. In consequence, it is reasonable for DM to have a fine-tuned oxidation potential, leading to better energy-level matching with the perovskite and a higher V_{OC} value in the device. As a part of our efforts to realize cost-effective HTM, we also introduced spiro[fluorene-9,9′-xanthene] as a recently reported low-cost core into DM, instead of spirobifluorene (see Supplementary Figs. 17–19)[24]. The synthesized spiro[fluorene-9,9′-xanthene]-based HTM with a peripheral dimethylfluorene moiety also exhibited a satisfying efficiency of 21.5% (see Supplementary Fig. 20).

Thermal and operational stability

To examine the thermal stability of the device prepared with DM, we investigated the thermal behaviour of a pristine HTM and an additive-doped HTM in a powder state using differential scanning calorimetry (DSC) in a simulation, as shown in Fig. 1e and Fig. 4a. The observed T_g of ~161 °C for the pristine DM powder is considerably reduced to ~90 °C after doping with the additives. This is most likely due to the role of liquid-type *t*BP as a plasticizer. A similar trend for spiro-OMeTAD can be found in the literature; doping with an additive into a pristine powder led to a significant drop in T_g from ~120 to ~50 °C (ref. [32]). Moreover, it was reported that the T_g values of organic semiconductors can be reduced in the thin-film state as compared to the bulk state[35]. It is known that deformation of spiro-OMeTAD film arises from crystallization after thermal annealing at a high temperature. For this reason, the device made with additive-doped spiro-OMeTAD exhibited apparent degradation when thermal annealing was applied from 60 °C to 80 °C in air (~25% relative humidity, RH) (Fig. 4b). In contrast, though slight degradation of the device was observed after thermal stress at 80 °C, the device with DM exhibited much better stability under an identical condition than the device with spiro-OMeTAD. Even after thermal stress at 60 °C for 500 h, the device performance was maintained at ~95% of the original value (see Fig. 4c). This is good evidence that our strategy of using a HTM with a high T_g value is feasible in PSCs, even if a higher T_g value of the HTM is still required for better thermal stability of the device. Furthermore, the encapsulated device using DM is also highly stable, with PCE maintaining 92.6% of its initial value after 310 h under continuous illumination condition (see Fig. 4d and Supplementary Fig. 21).

In conclusion, we have demonstrated highly efficient and thermally stable PSCs by employing a fluorene-terminated DM that has a HOMO energy level well matched to perovskite along with a high glass transition temperature (T_g). We fabricated a DM-based device and achieved high PCE values of 23.2% and 21.7% for small- (~0.094 cm^2) and large-area (~1 cm^2) cells, respectively, due to the significant reduction of the voltage loss of the device. The outcomes here were certified at 22.6% and 20.9% for small- and large-area cells, respectively. Furthermore, the device with DM showed better thermal stability than the device with spiro-OMeTAD, maintaining almost ~95% of its initial performance for more than 500 h after thermal annealing at 60 °C. We firmly believe that our fluorene-terminated DM created via molecular engineering is a promising HTM candidate for the fabrication of highly efficient and thermally stable PSCs and that our strategy in this work will offer a new direction for the fabrication of highly efficient and stable PSCs.

Methods

Materials. For synthesis of DM, tris(dibenzylideneacetone)dipalladium(0) was purchased from Strem Chemicals Inc. Tri-tert-butylphosphine was purchased from Kanto Chemical Co. Inc. 2,2′,7,7′-tetrabromo-9,9′-spirobi[9H-fluorene] was purchased from TCI Co. Ltd. 2-bromo-9,9-dimethylfluorene and all other reagents were purchased from Sigma-Aldrich. To fabricate the perovskite photoactive layer, formamidine acetate was purchased from Alfa Aesar and lead iodide and lead bromide were purchased from TCI Co. Ltd. All of the purchased chemicals were used as received without further purification.

Synthesis procedures of DM. Synthesis of N^2,$N^{2'}$,N^7,$N^{7'}$-tetrakis(4-methoxyphenyl)-9,9′-spirobi[fluorene]-2,2′,7,7′-tetraamine (Compound 1) proceeds as follows. In a 250 ml two-necked flask, 2,2′,7,7′-tetrabromo-9,9′-spirobi[9H-fluorene] (3 g, 4.75 mmol), *p*-anisidine (5.85 g, 47.47 mmol), sodium tert-butoxide (3.65 g, 37.97 mmol), tris(dibenzylideneacetone)dipalladium(0) (1.30 g, 1.42 mmol), tri-tert-butylphosphine (0.58 g, 2.85 mmol) were mixed. Next, anhydrous toluene was added into the flask, and the reaction mixture was heated to reflux at 130 °C for 30 h under a nitrogen atmosphere. After cooling to room temperature, the reaction mixture was extracted with ethyl acetate and brine water, and dried over anhydrous $MgSO_4$. After evaporation of the solvent, the residue was further purified by column chromatography (ethyl acetate/hexane = 40%) to afford a product as a powder in 58% yield (2.16 g).

^{1}H-NMR ($CDCl_3$, 400 MHz) $\delta = 7.34$ (d, 4H), 6.84 (s, 4H), 6.81 (d, 8H), 6.67 (d, 8H), 6.19 (s, 4H), 5.29 (s, 4H), 3.67 (s, 12H)

^{13}C-NMR ($CDCl_3$, 500 MHz) $\delta = 171.08$, 154.71, 150.64, 143.68, 136.10, 133.89, 121.24, 119.28, 114.53, 112.62, 60.36, 55.45, 20.97, 14.18

Synthesis of N^2,$N^{2'}$,N^7,$N^{7'}$-tetrakis(9,9-dimethyl-9H-fluoren-2-yl)-N^2,$N^{2'}$,N^7,$N^{7'}$-tetrakis(4-methoxyphenyl)-9,9′-spirobi[fluorene]-2,2′,7,7′-tetraamine (DM) proceeds as follows. In a 250 ml two-necked flask, Compound 1 (1.30 g, 1.6178 mmol), 2-bromo-9,9-dimethylfluorene (2.21 g, 8.09 mmol), sodium tert-butoxide (0.62 g, 6.47 mmol), tris(dibenzylideneacetone)dipalladium(0) (0.44 g, 0.49 mmol), tri-tert-butylphosphine (0.20 g, 0.97 mmol) were mixed. Next, anhydrous toluene was added into the flask. The reaction mixture was heated to reflux at 130 °C for 30 h under a nitrogen atmosphere. After cooling to room temperature, the reaction mixture was extracted with ethyl acetate and brine water, and dried over anhydrous $MgSO_4$. After evaporation of the solvent, the residue was further purified by column chromatography (ethyl acetate/hexane = 20%) to afford a product as a powder in 51% yield (1.30 g).

^{1}H-NMR (Acetone, 400 MHz) $\delta = 7.65$ (d, 4H), 7.60 (d, 4H), 7.43 (d, 8H), 7.21 (m, 8H), 7.19 (s, 4H), 7.07 (d, 8H), 6.91 (d, 8H), 6.86 (d, 4H), 6.81 (d, 4H), 6.67 (s, 4H), 3.80 (s, 12H), 1.33 (s, 24H)

^{13}C-NMR (Acetone, 400 MHz) $\delta = 158.55$, 156.64, 155.18, 151.84, 149.26, 149.06, 142.25, 140.67, 137.08, 135.24, 129.36, 128.86, 128.30, 124.39, 123.77, 123.65, 122.48, 121.97, 121.17, 118.97, 118.41, 116.71, 67.62, 56.72, 48.39, 28.54.

Synthesis procedures of SFX-DM. Synthesis of *N*-(4-methoxyphenyl)-9,9-dimethyl-9H-fluoren-2-amine (Compound 2) proceeds as follows. In a 250 ml two-necked flask, 2-bromo-9,9-dimethylfluorene (3 g, 10.982 mmol), *p*-Anisidine (1.62 g, 13.178 mmol), sodium tert-butoxide (2.11 g, 21.964 mmol), tris(dibenzylideneacetone)dipalladium(0) (1.01 g, 1.098 mmol), tri-tert-butylphosphine (0.44 g, 2.196 mmol) were mixed. Next, anhydrous toluene was added into the flask. The reaction mixture was heated to reflux at 130 °C for 30 h under a nitrogen atmosphere. After cooling to room temperature, the reaction mixture was extracted with ethyl acetate and brine water, and dried over anhydrous $MgSO_4$. After the solvent was evaporated, the residue was purified by column chromatography (ethyl acetate/hexane = 40%) to afford a powder in 75% yield (2.6 g).

^{1}H-NMR (Acetone, 400 MHz) $\delta = 7.59$ (d, 2H), 7.42 (d, 1H), 7.26 (t, 1H), 7.20 (s, 1H), 7.15 (m, 4H), 6.96 (d, 1H), 6.90 (d, 2H), 3.77 (s, 3H), 1.43 (s, 6H)

Synthesis of N^2,N^7-bis(9,9-dimethyl-9H-fluoren-2-yl)-N^2,N^7-bis(4-methoxyphenyl)spiro [fluorene-9,9′-xanthene]-2,7-diamine (SFX-DM) proceeds as follows. In a 250 ml two-necked flask, Compound 2 (1.42 g, 4.49 mmol), 2,7-dibromospiro[fluorene-9,9′-xanthene] (1.00 g, 2.040 mmol), sodium tert-butoxide (0.980 g, 10.200 mmol), tris(dibenzylideneacetone)dipalladium(0) (0.37 g, 0.408 mmol), tri-tert-butylphosphine (0.17 g, 0.816 mmol) were mixed. Next,

anhydrous toluene was added into the flask. The reaction mixture was heated to reflux at 130 °C for 30 h under a nitrogen atmosphere. After cooling to room temperature, the reaction mixture was extracted with ethyl acetate and brine water, and dried over anhydrous $MgSO_4$. After the solvent was evaporated, the residue was purified by column chromatography (ethyl acetate/hexane = 20%) to afford a powder in 66% yield (1.29 g).
^{1}H-NMR (Acetone, 400 MHz) δ = 7.72 (d, 2H), 7.63 (d, 2H), 7.53 (d, 2H), 7.41 (d, 2H), 7.24 (m, 3H), 7.20 (d, 2H), 7.16 (d, 2H), 7.08 (s, 2H), 6.99 (m, 6H), 6.94 (d, 3H), 6.85 (m, 6H), 6.77 (d, 2H), 6.63 (d, 2H), 3.78 (s, 6H), 1.20 (s, 12H)
^{13}C-NMR (Acetone, 400 MHz) δ = 156.63, 156.44, 154.85, 153.36, 150.96, 147.87, 147.39, 140.39, 138.85, 133.44, 128.31, 127.90, 127.26, 126.95, 126.39, 124.85, 123.49, 122.44, 122.22, 122.04, 120.62, 120.18, 119.27, 118.86, 117.01, 116.64, 114.81, 54.83, 54.01, 46.43, 26.52.

Device fabrication. A dense blocking layer of TiO_2 (bl-TiO_2) was deposited onto a FTO (Pilkington, TEC8) substrate by spray pyrolysis deposition carried out using a 20 mM titanium diisopropoxide bis(acetylacetonate) solution (Sigma-Aldrich) at 450 °C. Subsequently, mesoporous TiO_2 (mp-TiO_2) films were spin-coated onto the bl-TiO_2/FTO substrate using diluted commercial paste (SC-HT040, ShareChem) and were calcined at 500 °C for 1 h in air to remove the organic portion. To fabricate perovskite solar cells based on $(FAPbI_3)_{0.95}(MAPbBr_3)_{0.05}$, the perovskite solution was prepared by dissolving 889 mg ml^{-1} of $FAPbI_3$, 33 mg ml^{-1} of $MAPbBr_3$ and 33 mg ml^{-1} of MACl in DMF/DMSO (8:1 v/v) mixed solvent. Then, the solution was coated onto the mp-TiO_2/*bl*-TiO_2/FTO substrate by two consecutive spin-coating steps, at 1,000 and 5,000 r.p.m. for 5 s and 20 s, respectively. During the second spin-coating (5,000 r.p.m.) step, 1 ml of ethyl ether was poured onto the substrate after 15 s. The intermediate phase substrate was then put on a hot plate at 150 °C for 10 min. For deposition of hole-transport materials, a spiro-OMeTAD solution in chlorobenzene (CB) (90.9 mg ml^{-1}) was prepared, and 23 μl of lithium-bis(trifluoromethanesulfonyl) imide (Li-TFSI) solution in acetonitrile (ACN) (540 mg ml^{-1}) and 39 μl of pure 4-*tert*-butylpyridine (*t*BP) were added in 1.1 ml of the solution. The spiro-OMeTAD solution including additives was spin-coated onto the perovskite surface at 4,000 r.p.m. for 30 s. In the case of DM, a DM solution in CB (28.6 mg ml^{-1}) was prepared, and 0–9 μl of Li-TFSI solution in ACN (340 mg ml^{-1}) and 0–9 μl of pure *t*BP (no dilution) were added in 0.35 ml of the solution. The added volume ratio of Li-TFSI solution and pure *t*BP is 1:1. The DM solution including additives was spin-coated onto the perovskite surface at 2,000 r.p.m. for 30 s. Finally, a Au counter electrode was deposited by thermal evaporation.

Characterizations and measurements. The *J*–*V* curves were measured using a solar simulator (Newport, Oriel Class A, 91195 A) with a source meter (Keithley 2420) at a size of 100 mA cm^{-2} under illumination at AM 1.5 G and a calibrated Si-reference cell certified by NREL. The *J*—*V* curves were measured along the reverse scan direction from 1.5 V to −0.2 V or the forward scan direction from −0.2 V to 1.5 V. The step voltage and scan speed were fixed at 10 mV and 150 mV s^{-1}, respectively. The *J*–*V* curves for all devices were measured by metal masks with active areas of 0.0939 cm^2 (small-area device) and 0.991 cm^2 (large-area device) in size. Electrochemical properties of the HTMs were investigated by three-electrode cyclic voltammetry (CV) using a BAS 100B electrochemical analyser. DM or spiro-OMeTAD was dissolved in 0.1 M methylene chloride solution of tetrabutylammonium hexafluorophosphate. Two platinum electrodes were used as working electrode and counter electrode, respectively, and Ag/Ag$^+$ was used as reference electrode. The scanning rate was 50 mV s^{-1}, and the measured potentials were calibrated using ferrocene as an internal standard. Time-resolved photoluminescence (TRPL) decay profiles were measured at 800 nm with the 532 nm excitation of an OPO laser system (NT 342A-10-AW, EKSPLA). The pulse energy was strongly attenuated to less than 1 μJ, to avoid nonlinear effects such as exciton–exciton annihilation. Emissions from samples were collected by a monochromator (SP2150, Princeton Instruments) equipped with a photomultiplier tube (PMT) (Hamamatsu, H10721-20). The output signal from a PMT was recorded with a 500 MHz digital oscilloscope (DSO-X 3054 A, Agilent). For estimating the valence band maxima of the perovskites and the ionization potentials of the HTMs, photoelectron spectroscopy (PES) measurements were performed using a Riken Keiki AC-2 photoelectron spectrometer in air. SEM images were obtained using a Tescan Mira 3 LMU FEG field-emission scanning electron microscope. The XRD was measured by the Rigaku Ultima IV X-ray diffractometer using Cu Ka radiation. Transient photovoltage decay measurements were taken using a nanosecond laser (EKSPLA, NT342A-10) as a small perturbation light source and a Xe lamp (Zolix, 150 W) as a bias light source. The device was directly connected to a digital oscilloscope (Agilent, DSO-X 3054 A) with the input impedance of the oscilloscope set to 1 MΩ for an open-circuit condition. The bias light intensity was controlled by a neutral density filter set for various open-circuit voltages (V_{oc}) and a strongly attenuated laser pulse of 550 nm was used to generate a voltage transient (ΔV) of less than 20 mV.

Device stability test. Thermal stability tests were performed by aging an encapsulated device with increasing temperature (at 60 °C, 70 °C and 80 °C for 50 h, respectively) on a hot plate in ambient air (~25% RH). PCE of the device was periodically measured under AM1.5 G simulated sun light after cooling the device down to room temperature. Long-term thermal stability tests were carried out at 60 °C for 500 h on a hot plate in ambient air, and PCE was periodically recorded under AM1.5 G simulated sun light at room temperature. All of devices for thermal stability test were stored in dark conditions. Maximum power point tracking (MPPT) was also carried out to verify the long-term photostability. The maximum power point of the encapsulated device under AM1.5 G simulated LED light (LSH-7320, Newport, USA) was measured by using a source meter (Keithley 2420, USA) operated by self-written software using a perturb-observe algorithm. The environmental conditions were maintained at a temperature of 25 °C and a relative humidity of 25% RH. The temperature of the devices was maintained between 30 and 40 °C by air cooling. The devices were encapsulated using a getter-dispersed polymer barrier under a nitrogen atmosphere. Finally, those were covered with thermally curable epoxy resin and cover glass.

Data availability. The data that support the plots within this paper and other findings of this study are available from the corresponding authors upon reasonable request.

Received: 28 January 2018; Accepted: 8 June 2018;

References

1. Stranks, S. D. et al. Electron-hole diffusion lengths exceeding 1 micrometer in an organometal trihalide perovskite absorber. *Science* **342**, 341–344 (2013).
2. Zhao, Y. & Zhu, K. Organic-inorganic hybrid lead halide perovskites for optoelectronic and electronic applications. *Chem. Soc. Rev.* **45**, 655–689 (2016).
3. Xing, G. et al. Long-range balanced electron- and hole-transport lengths in organic–inorganic $CH_3NH_3PbI_3$. *Science* **342**, 344–347 (2013).
4. Snaith, H. J. Perovskites: The emergence of a new era for low-cost, high-efficiency solar cells. *J. Phys. Chem. Lett.* **4**, 3623–3630 (2013).
5. Park, N.-G., Grätzel, M., Miyasaka, T., Zhu, K. & Emery, K. Towards stable and commercially available perovskite solar cells. *Nat. Energy* **1**, 16152 (2016).
6. Jeon, N. J. et al. Solvent engineering for high-performance inorganic–organic hybrid perovskite solar cells. *Nat. Mater.* **13**, 897–903 (2014).
7. Jeon, N. J. et al. Compositional engineering of perovskite materials for high-performance solar cells. *Nature* **517**, 476–480 (2015).
8. Yang, W. S. et al. High-performance photovoltaic perovskite layers fabricated through intramolecular exchange. *Science* **348**, 1234–1237 (2015).
9. Yang, W. S. et al. Iodide management in formamidinium–lead-halide-based perovskite layers for efficient solar cells. *Science* **356**, 1376–1379 (2017).
10. *Best Research-Cell Efficiencies* (NREL, 2016); https://www.nrel.gov/pv/assets/images/efficiency-chart.png.
11. Wang, Z. et al. Efficient ambient-air-stable solar cells with 2D–3D heterostructured butylammonium-caesium-formamidinium lead halide perovskites. *Nat. Energy* **2**, 17135 (2017).
12. Saliba, M. et al. Cesium-containing triple cation perovskite solar cells: improved stability, reproducibility and high efficiency. *Energy Environ. Sci.* **9**, 1989–1997 (2016).
13. Grätzel, M. The rise of highly efficient and stable perovskite solar cells. *Acc. Chem. Res.* **50**, 487–491 (2017).
14. Rehman, W. et al. Photovoltaic mixed-cation lead mixed-halide perovskites: links between crystallinity, photo-stability and electronic properties. *Energy Environ. Sci.* **10**, 361–369 (2017).
15. Saliba, M. et al. Incorporation of rubidium cations into perovskite solar cells improves photovoltaic performance. *Science* **354**, 206–209 (2016).
16. Shao, Y., Xiao, Z., Bi, C., Yuan, Y. & Huang, J. Origin and elimination of photocurrent hysteresis by fullerene passivation in $CH_3NH_3PbI_3$ planar heterojunction solar cells. *Nat. Commun.* **5**, 5784 (2014).
17. Nie, W. et al. High-efficiency solution-processed perovskite solar cells with millimeter-scale grains. *Science* **347**, 522–525 (2015).
18. Son, D.-Y. et al. Self-formed grain boundary healing layer for highly efficient $CH_3NH_3PbI_3$ perovskite solar cells. *Nat. Energy* **1**, 16081 (2016).
19. Tsai, H. et al. High-efficiency two-dimensional Ruddlesden–Popper perovskite solar cells. *Nature* **536**, 312–316 (2016).
20. Polander, L. E. et al. Hole-transport material variation in fully vacuum deposited perovskite solar cells. *APL Mater.* **2**, 081503 (2014).
21. Arora, N. et al. High open-circuit voltage: Fabrication of formamidinium lead bromide perovskite solar cells using fluorene–dithiophene derivatives as hole-transporting materials. *ACS Energy Lett.* **1**, 107–112 (2016).
22. Chen, H. et al. Molecular engineered hole-extraction materials to enable dopant-free, efficient p-i-n perovskite solar cells. *Adv. Energy Mater.* **7**, 1700012 (2017).
23. Saliba, M. et al. A molecularly engineered hole-transporting material for efficient perovskite solar cells. *Nat. Energy* **1**, 15017 (2016).
24. Bi, D. et al. Facile synthesized organic hole transporting material for perovskite solar cell with efficiency of 19.8%. *Nano Energy* **23**, 138–144 (2016).

25. Xu, B. et al. Tailor-making low-cost spiro[fluorene-9,9′-xanthene]-based 3D oligomers for perovskite solar cells. *Chem* **2**, 676–687 (2017).
26. Malinauskas, T. et al. Branched methoxydiphenylamine-substituted fluorene derivatives as hole transporting materials for high-performance perovskite solar cells. *Energy Environ. Sci.* **9**, 1681–1686 (2016).
27. Kim, G.-W., Lee, J., Kang, G., Kim, T. & Park, T. Donor–acceptor type dopant-free, polymeric hole transport material for planar perovskite solar cells (19.8%). *Adv. Energy Mater*. **8**, 1701935 (2018).
28. Hawash, Z., Ono, L. K. & Qi, Y. Photovoltaics: Recent advances in spiro-MeOTAD hole transport material and its applications in organic–inorganic halide perovskite solar cells. *Adv. Mater. Interfaces* **5**, 1700623 (2018).
29. Zhao, X. & Wang, M. Organic hole-transporting materials for efficient perovskite solar cells. *Mater. Today Energy* **7**, 208–220 (2017).
30. Cho, I. et al. Indolo[3,2-b]indole-based crystalline hole-transporting material for highly efficient perovskite solar cells. *Chem. Sci.* **8**, 734–741 (2017).
31. Zhao, X., Kim, H.-S., Seo, J.-Y. & Park, N.-G. Effect of selective contacts on the thermal stability of perovskite solar cells. *ACS Appl. Mater. Interfaces* **9**, 7148–7153 (2017).
32. Malinauskas, T. et al. Enhancing thermal stability and lifetime of solid-state dye-sensitized solar cells via molecular engineering of the hole-transporting material Spiro-OMeTAD. *ACS Appl. Mater. Interfaces* **7**, 11107–11116 (2015).
33. Jeon, N. J. et al. *o*-Methoxy substituents in spiro-OMeTAD for efficient inorganic–organic hybrid perovskite solar cells. *J. Am. Chem. Soc.* **136**, 7837–7840 (2014).
34. Hu, Z. et al. Effects of heteroatom substitution in spiro-bifluorene hole transport materials. *Chem. Sci.* **7**, 5007–5012 (2016).
35. Komino, T., Nomura, H., Yahiro, M. & Adachi, C. Real-time measurement of molecular orientational randomization dynamics during annealing treatments by in-situ ellipsometry. *J. Phys. Chem. C.* **116**, 11584–11588 (2012).

Acknowledgements

This work was supported by a grant from the Korea Research Institute of Chemical Technology (KRICT), Republic of Korea (KK1802-A01), the Korea Institute of Energy Technology Evaluation and Planning (KETEP) and the Ministry of Trade Industry & Energy (MOTIE) of the Republic of Korea (No. 20163010012470), and by a grant from the National Research Foundation of Korea (NRF) funded by the Ministry of Science, ICT & Future Planning (MSIP) of Korea (NRF-2016M3A6A7945503). This research was also supported by the Basic Science Research Program through the National Research Foundation of Korea (NRF) funded by the Ministry of Education (NRF-2015R1A6A3A04058164).

Author contributions

J.S. and J.L. conceived and supervised the project. N.J.J., E.H.J., S.I.S., J.S. and J.L. wrote the paper. N.J.J. and E.H.J. fabricated and characterized the perovskite solar cells. N.J.J., E.H.J. and J.S. achieved the certified performance of devices at Newport Corporation. H.N. synthesized the relevant materials. H.N. and Y.G.L. performed analysis of the intrinsic properties of the materials via DFT calculation, ultraviolet–visible absorption, CV, TGA, DSC and SCLC measurements. N.J.J. and E.H.J. carried out SEM measurements. T.Y.Y. and H.W.S. analysed charge recombination lifetimes via transient photovoltage measurements as a function of the bias light intensity. G.K. performed TRPL measurements. All authors discussed the results.

Competing interests

The authors declare no competing interests.

Additional information

Supplementary information is available for this paper at https://doi.org/10.1038/s41560-018-0200-6.

Reprints and permissions information is available at www.nature.com/reprints.

Correspondence and requests for materials should be addressed to J.L. or J.S.

nature research

Corresponding author(s): Jaemin Lee and Jangwon Seo

Solar Cells Reporting Summary

Nature Research wishes to improve the reproducibility of the work that we publish. This form is intended for publication with all accepted papers reporting the characterization of photovoltaic devices and provides structure for consistency and transparency in reporting. Some list items might not apply to an individual manuscript, but all fields must be completed for clarity.

For further information on Nature Research policies, including our data availability policy, see Authors & Referees.

▸ Experimental design

Please check: are the following details reported in the manuscript?

1. Dimensions

Area of the tested solar cells	☒ Yes ☐ No	Section "Characterizations and measurements" & Supplementary Figure 10 and 11
Method used to determine the device area	☐ Yes ☒ No	The area of our masks was determined and certified at Newport corporation. However, we do not have the detailed information for the method.

2. Current-voltage characterization

Current density-voltage (J-V) plots in both forward and backward direction	☒ Yes ☐ No	Figure 2b, c
Voltage scan conditions *For instance: scan direction, speed, dwell times*	☒ Yes ☐ No	Section "Characterizations and measurements"
Test environment *For instance: characterization temperature, in air or in glove box*	☐ Yes ☒ No	Our devices were characterized at room temperature (ca. 25 Celsius degree) in air. And see Section "Device stability test".
Protocol for preconditioning of the device before its characterization	☐ Yes ☒ No	No preconditioning protocol.
Stability of the J-V characteristic *Verified with time evolution of the maximum power point or with the photocurrent at maximum power point; see ref. 7 for details.*	☒ Yes ☐ No	Supplementary Figure 9

3. Hysteresis or any other unusual behaviour

Description of the unusual behaviour observed during the characterization	☒ Yes ☐ No	Section "Photovoltaic performance"
Related experimental data	☒ Yes ☐ No	Figure 2b, c & Supplementary Figure 10 and 11

4. Efficiency

External quantum efficiency (EQE) or incident photons to current efficiency (IPCE)	☒ Yes ☐ No	Supplementary Figure 10 and 11
A comparison between the integrated response under the standard reference spectrum and the response measure under the simulator	☒ Yes ☐ No	Supplementary Figure 10 and 11
For tandem solar cells, the bias illumination and bias voltage used for each subcell	☐ Yes ☒ No	Our devices were only fabricated for single solar cells.

5. Calibration

Light source and reference cell or sensor used for the characterization	☒ Yes ☐ No	Section "Characterizations and measurements"
Confirmation that the reference cell was calibrated and certified	☒ Yes ☐ No	Section "Characterizations and measurements"

Calculation of spectral mismatch between the reference cell and the devices under test	☒ Yes ☐ No	The spectral mismatch factor (M) was determined by PV Lab of Technology and Application Center in Newport Corporation. See Supplementary Figure 10 and 11.

6. Mask/aperture

Size of the mask/aperture used during testing	☒ Yes ☐ No	Section "Charaterizations and measurements" & Supplementary Figure 10 and 11
Variation of the measured short-circuit current density with the mask/aperture area	☒ Yes ☐ No	Figure 2b, c & Supplementary Figure 10 and 11

7. Performance certification

Identity of the independent certification laboratory that confirmed the photovoltaic performance	☒ Yes ☐ No	Our devices were certified at PV Lab of Technology and Application Center in Newport Corporation.
A copy of any certificate(s) *Provide in Supplementary Information*	☒ Yes ☐ No	Copies of certificates can be found in Supplementary Figure 10 for a small-area device (0.0939 cm2) and Supplementary Figure 11 for large-area device (0.919 cm2).

8. Statistics

Number of solar cells tested	☒ Yes ☐ No	Caption "Figure 2d", "Figure 3c" & "Supplementary Figure 16"
Statistical analysis of the device performance	☒ Yes ☐ No	Section "Photovoltaic performance", Figure 2d, Figure 3c & Supplementary Figure 16

9. Long-term stability analysis

Type of analysis, bias conditions and environmental conditions *For instance: illumination type, temperature, atmosphere humidity, encapsulation method, preconditioning temperature*	☒ Yes ☐ No	Section "Thermal and operational stability" and "Device stability test", Figure 4 & Supplementary Figure 21